

Anomalous ultrafast thermalization of photoexcited carriers in two-dimensional materials induced by orbital coupling

Zhuoqun Wen(文卓群), Haiyu Zhu(诸海渝), Wen-Hao Liu(刘文浩), Zhi Wang(王峙), Wen Xiong(熊稳), and Xingzhan Wei(魏兴战)

Citation: Chin. Phys. B, 2025, 34 (**7**): 077103. DOI: 10.1088/1674-1056/adc191
http://cpb.iphy.ac.cn; http://iopscience.iop.org/cpb

What follows is a list of articles you may be interested in

Unveiling the thermal transport mechanisms in novel carbon-based graphene-like materials using machine-learning potential

Yao-Yuan Zhang(章耀元), Meng-Qiu Long(龙孟秋), Sai-Jie Cheng(程赛杰), and Wu-Xing Zhou(周五星)
Chin. Phys. B, 2025, 34 (**6**): 067101. DOI: 10.1088/1674-1056/adca18

Actively tuning anisotropic light—matter interaction in biaxial hyperbolic material α-MoO_3 using phase change material VO_2 and graphene

Kun Zhou(周昆), Yang Hu(胡杨), Biyuan Wu(吴必园), Xiaoxing Zhong(仲晓星), and Xiaohu Wu(吴小虎)
Chin. Phys. B, 2024, 33 (**4**): 047103. DOI: 10.1088/1674-1056/ad23d2

Effects of vacancy and external electric field on the electronic properties of the $MoSi_2N_4$/graphene heterostructure

Qian Liang(梁前), Xiangyan Luo(罗祥燕), Guolin Qian(钱国林), Yuanfan Wang(王远帆), Yongchao Liang(梁永超), and Quan Xie(谢泉)
Chin. Phys. B, 2024, 33 (**3**): 037101. DOI: 10.1088/1674-1056/acef04

Atomistic simulations of graphene origami: Dynamics and kinetics

Panpan Zhang(张盼盼), Haihong Jia(贾海洪), Yan-Fang Zhang(张艳芳), and Shixuan Du(杜世萱)
Chin. Phys. B, 2023, 32 (**8**): 087107. DOI: 10.1088/1674-1056/acd527

Plasmonic hybridization properties in polyenes octatetraene molecules based on theoretical computation

Nan Gao(高楠), Guodong Zhu(朱国栋), Yingzhou Huang(黄映洲), and Yurui Fang(方蔚瑞)
Chin. Phys. B, 2023, 32 (**3**): 037102. DOI: 10.1088/1674-1056/ac891c

---

Anomalous ultrafast thermalization of photoexcited carriers in two-dimensional materials induced by orbital coupling

Zhuoqun Wen(文卓群)[1,2,3], Haiyu Zhu(诸海渝)[2,4], Wen-Hao Liu(刘文浩)[5], Zhi Wang(王峙)[5,†], Wen Xiong(熊稳)[1,2,‡], and Xingzhan Wei(魏兴战)[1,2,3,§]

[1] *Chongqing Institute of Green and Intelligent Technology, Chinese Academy of Sciences, Chongqing* 400714, *China*
[2] *Chongqing School, University of Chinese Academy of Sciences, Chongqing* 400714, *China*
[3] *University of Chinese Academy of Sciences, Beijing* 100049, *China*
[4] *School of Optoelectronic Engineering, Chongqing University of Posts and Telecommunications, Chongqing* 400065, *China*
[5] *State Key Laboratory of Semiconductor Physics and Chip Technologies, Institute of Semiconductors, Chinese Academy of Sciences, Beijing* 100083, *China*

(Received 17 January 2025; revised manuscript received 6 March 2025; accepted manuscript online 18 March 2025)

Understanding the dynamics of photoexcited carriers is essential for advancing photoelectronic device design. Photon absorption generates electron–hole pairs, and subsequent scatterings can induce ultrafast thermalization within a picosecond, forming a quasi-equilibrium distribution with overheated electrons. The high-energy tail of this distribution enables carriers to overcome energy barriers, thereby enhancing quantum efficiency — a phenomenon known as photothermionic emission (PTE). Despite its importance, the onset and mechanisms of PTE remain under debate. Using real-time time-dependent density functional theory (rt-TDDFT), we investigate ultrafast carrier thermalization in two-dimensional (2D) materials graphene and $PtTe_2$, and the results reveal distinct differences. In graphene, both electrons and holes thermalize into Fermi–Dirac distributions with good agreement to experiment, while $PtTe_2$ exhibits anomalous high-energy tails for both electrons and holes, deviating significantly from Fermi–Dirac behavior. We attribute this anomaly to differences in orbital coupling between the two materials, from which we derive design principles for identifying optimal PTE candidates and, ultimately, improving photodetector performance.

Keywords: ultrafast phenomena, time-dependent density functional theory, photoelectronics, photothermionic emission, 2D materials, graphene, platinum ditelluride

PACS: 71.15.Mb, 87.15.ht

DOI: 10.1088/1674-1056/adc191 **CSTR:** 32038.14.CPB.adc191

1. Introduction

Enhancing the performance of photodetectors remains one of the central goals in modern photoelectronics. Within the conventional perspective, two primary mechanisms are recognized for photon detection: (i) photon energy exceeding the band gap of a semiconductor, leading to a direct photoelectronic absorption, or (ii) photoexcited carriers with energy surpassing the Schottky barrier at the interface of metal-semiconductor junction, generating a photocurrent. The latter mechanism, known as the internal photoemission (IPE) effect, has been pivotal in the development of visible and near-infrared photodetectors.[1–3] The efficiency and spectral response range of photodetectors are hence fundamentally constrained by the Schottky barrier height. However, recent experiments on heterojunction devices of two-dimensional (2D) materials, particularly graphene–silicon systems, have challenged this limitation. These systems demonstrated substantial photocurrent responses to long-wavelength infrared radiation, even in the presence of high Schottky barriers.[4–8] The PTE effect has been proposed to explain this discrepancy.[9–13] Being observed in ultrafast transient measurements of graphene,[14,15] PTE describes a non-equilibrium process in which the photoexcited carriers undergo ultrafast thermalization via electron–electron (or hole–hole) scattering, forming quasi-equilibrium distributions, e.g., a Fermi–Dirac distribution, within sub-picoseconds. The high-energy tail of this distribution enables carriers to overcome energy barriers, thereby generating photocurrent and enhancing quantum efficiency. The two-temperature model (TTM), in which electrons can have a high temperature while the lattice remains relatively cool, has been widely adopted to describe such system, and the energy transfer through the electron–phonon coupling gradually restores the thermal equilibrium between electrons and the lattice over a longer timescale.[16–18]

While the TTM has been successful in describing photoelectronic processes in graphene-based heterostructures, questions remain about its general applicability. Specifically, is the Fermi–Dirac distribution always valid and "temperature" always well-defined across different sys-

†Corresponding author. E-mail: wangzhi@semi.ac.cn
‡Corresponding author. E-mail: xiongwen@cigit.ac.cn
§Corresponding author. E-mail: weixingzhan@cigit.ac.cn

© 2025 Chinese Physical Society and IOP Publishing Ltd. All rights, including for text and data mining, AI training, and similar technologies, are reserved.

tems? More importantly, how and when can the carrier occupation in the high-energy tail be tuned to enhance photodetector efficiency? To address the complexities observed in ultrafast dynamics, extensions to the TTM have been developed.[19,20] These include non-thermal lattice models,[21,22] three-temperature models,[23] and alternative theoretical frameworks such as time-dependent Boltzmann equations,[24–29] master equations,[30] non-equilibrium Green's functions,[31,32] and TDDFT.[33–39] While conventional models primarily attribute the thermalization to electron–electron scattering,[14,40–43] alternative perspectives highlight the role of phonon interactions[44–47] or orbital coupling[35–37,48,49] in shaping carrier dynamics. Nonetheless, the lack of first-principles studies limits a comprehensive understanding of thermalization processes, and the mechanisms underlying the formation of overheated quasi-equilibrium distributions remain contentious.

In this study, we use rt-TDDFT[34] to investigate the ultrafast carrier thermalization dynamics in 2D materials, monolayer graphene and $PtTe_2$. We employ an approach[50] based on band-to-band transition coefficients to examine the time-resolved evolution of carrier distributions, not imposed *a priori* but computed directly from first-principles simulations. In graphene, we demonstrate that photoexcited carriers rapidly achieve a Fermi–Dirac distribution within ultrafast timescales, consistent with experimental observations. In contrast, in $PtTe_2$, we uncover significant deviations from Fermi–Dirac behavior in the distribution of photoexcited carriers, characterized by the presence of overheated electrons and holes. These anomalous thermalization effects are attributed to the distinctive orbital coupling mechanisms in $PtTe_2$ compared to graphene. We then propose design principles for identifying or engineering high-efficiency PTE materials based on orbital coupling and consistency, providing a roadmap for future material development.

2. Real-time time-dependent density functional theory

Our rt-TDDFT approach is designed to solve non-perturbative, non-linear dynamics in systems of hundreds of atoms over timescales ranging from femtoseconds to picoseconds.[34,50–52] The concepts of this method are elaborated in Ref. [34] and summarized as follows: The time-dependent electron wavefunctions $\{\psi_i(t)\}$, evolving according to the time-dependent Schrödinger equation $\mathrm{i}\partial\psi_i(t)/\partial t = H(t)\psi_i(t)$, can be expanded in terms of the adiabatic states $\{\phi_j(t)\}$,

$$\psi_i(t) = \sum_j C_{j,i}(t)\,\phi_j(t). \tag{1}$$

Here, $\{\phi_j(t)\}$ are eigenstates of time-dependent Hamiltonian, $H(t)\phi_j(t) = \varepsilon_j(t)\phi_j(t)$. The nuclear positions follow Newton's law, with forces derived from the total energy via Hellmann–Feynman theorem. In our rt-TDDFT implementation, electron–electron interactions are treated within a single-determinant framework as in conventional DFT approaches, i.e., in the Kohn–Sham potential including the exchange–correlation terms.

To analyze the carrier distribution, the time-dependent density of state $\mathrm{DOS}(\varepsilon,t)$ and time-dependent density of occupied state $\mathrm{Occ}(\varepsilon,t)$ at energy ε and time t are calculated as follows:

$$\mathrm{DOS}(\varepsilon,t) = g\sum_j \delta(\varepsilon-\varepsilon_j), \tag{2}$$

$$\mathrm{Occ}(\varepsilon,t) = \sum_j \delta(\varepsilon-\varepsilon_j)\sum_i \mathrm{Occ}^0\left(\varepsilon_i^0\right)\left|C_{j,i}(t)\right|^2, \tag{3}$$

where the summation over j runs over all adiabatic states, and the summation over i includes all time-dependent states. g is the spin degeneracy factor, $\mathrm{Occ}^0\left(\varepsilon_i^0\right)$ is the initial occupation on state i at time zero (before laser), $C_{j,i}(t)$ is the expansion coefficient in Eq. (1), and $\delta(\varepsilon-\varepsilon_j)$ is the Dirac δ function (substituted by a Gaussian function with a broadening factor in this work). The density of excited carriers at time t_1, $D_{\mathrm{exci}}(\varepsilon,t_1)$, can then be calculated by the difference between $\mathrm{Occ}(\varepsilon,0)$ and $\mathrm{Occ}(\varepsilon,t_1)$, which we mark as

$$D_{\mathrm{exci}}(\varepsilon,t_1) = \mathrm{Occ}(\varepsilon,t_1) - \mathrm{Occ}(\varepsilon,0). \tag{4}$$

D_{exci} can be either positive or negative, where positive values indicate excited electrons and negative ones indicate excited holes. The time-dependent distribution function of electrons $f(\varepsilon,t)$ is derived from the equation

$$\mathrm{Occ}(\varepsilon,t) = f(\varepsilon,t)\times\mathrm{DOS}(\varepsilon,t), \tag{5}$$

and the distribution function of excited carrier at time t_1, $f_{\mathrm{exci}}(\varepsilon,t_1)$, is defined as the difference between $f(\varepsilon,0)$ and $f(\varepsilon,t_1)$,

$$f_{\mathrm{exci}}(\varepsilon,t_1) = f(\varepsilon,t_1) - f(\varepsilon,0). \tag{6}$$

This approach ensures that the carrier distribution f is not imposed *a priori*, but is instead computed directly from first-principles simulations.

The DFT and rt-TDDFT simulations are implemented in the PWmat package. All runs have been calculated using norm-conserving pseudopotentials (NCPP) and Perdew–Burke–Ernzerhof (PBE) functional[53] (see the supplementary materials for details).

3. Results and discussion

3.1. Ground-state properties of graphene and $PtTe_2$

We first calculated the lattice constants and band structures for monolayer graphene and $PtTe_2$, and compared the results with previous literature. As summarized in Table 1, our

calculated lattice constants of graphene and $PtTe_2$ deviate from experimental values[54,55] by approximately 0.05% and 0.3%, respectively. Previous studies have extensively validated the DFT simulations for graphene.[56–59] In this work, we focus on the monolayer $PtTe_2$, and the calculated band structures for both graphene and $PtTe_2$ are presented in Fig. 1. The result reveals an indirect bandgap of 0.34 eV. Both the gap energy and the E versus $\boldsymbol{k}$ dispersion agree well with prior studies.[55,60–62]

Table 1. Comparisons of lattice constants of monolayer graphene and $PtTe_2$.

	This work	Previous theory	Experiment
Graphene	2.458 Å	2.4589 Å[56] 2.4595 Å[57] 2.46 Å[58]	2.4589 ± 0.0005 Å (297 K)[54]
$PtTe_2$	4.043 Å	4.05 Å (PBE+D3)[55] 4.1 Å (PBE+TS)[55] 4.06 Å (PBE+MBD)[55]	4.03 Å[55]

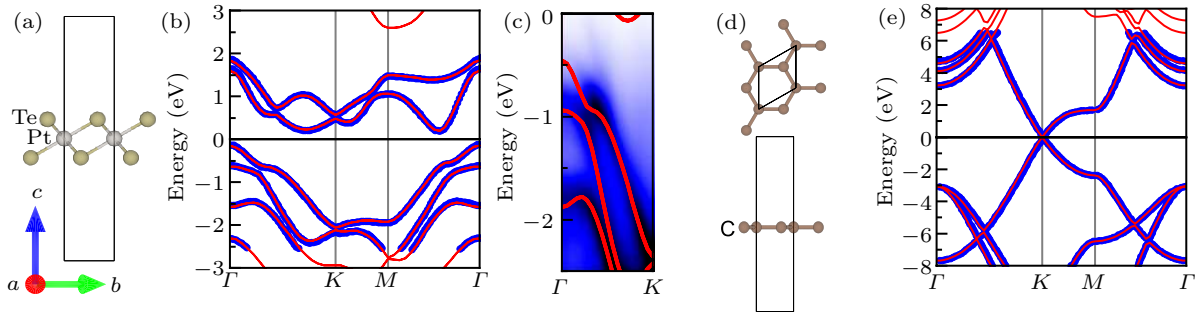


Fig. 1. Ground-state properties of monolayer $PtTe_2$ and graphene: (a) schematic diagram of $PtTe_2$ atomic structure, (b) comparisons of $PtTe_2$ band structures between this work (red) and the previous study in Ref. [55] (blue), (c) dispersive features of $PtTe_2$ along the Γ–K direction, showing a comparison between this work (red solid lines) and experimental ARPES data from Ref. [55] (black-blue-white colormap), (d) schematic diagram of graphene atomic structure, (e) comparisons of graphene band structures between this work (red) and the previous theoretical study in Ref. [63] (blue).

3.2. Photoexcited carrier thermalization in graphene

Using a laser field similar to the one reported in experiment Ref. [15] (See supplementary materials for details in the "computational parameters" section), we investigate the photoexcited carrier distributions $f_{\mathrm{exci}}(\varepsilon,t)$ obtained from TDDFT and compare them with the ones extracted from energy distribution curves reported in the same reference. Figure 2 illustrates the simulated distribution functions of the excited carriers from TDDFT. Both electrons and holes thermalize into well-defined Fermi–Dirac distributions, with goodness of fit $R^2 > 0.9$. Such quasi-equilibrium distributions are formed within 30 fs (Fig. 2(b)), a timescale aligns well with that from ultrafast experiment but significantly shorter than that typically required for electron–phonon coupling. The temperature of the excited electrons after 30 fs, extracted from the Fermi–Dirac fit, is approximately 3000 K, which is in good agreement with experimental results in Ref. [15]. The Fermi–Dirac behavior is maintained throughout the simulation (to 240 fs, Fig. 2(c)). While there is no evident cooling or recombination processes observed, suggesting that these phenomena may occur over longer timescales.

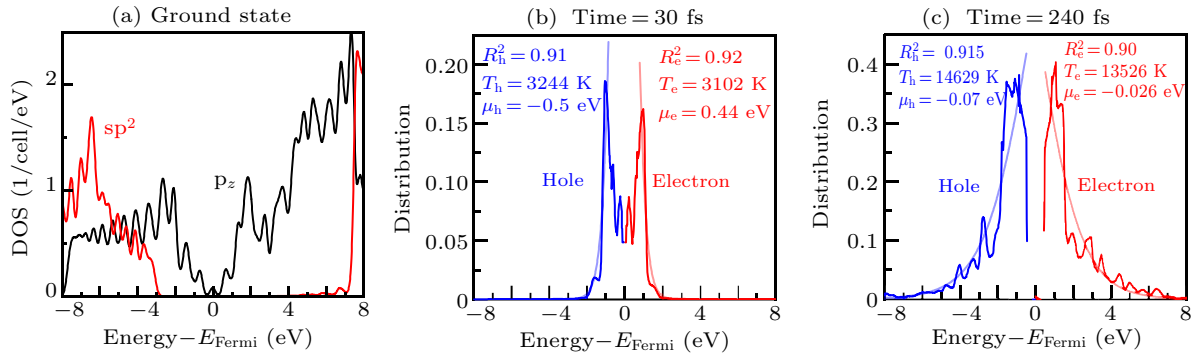


Fig. 2. Carrier distributions in monolayer graphene. (a) The calculated ground-state density of states of monolayer graphene, projected onto the in-plane, sp^2-hybrid orbital (red) and the out-of-plane p_z orbital (black). (b)–(c) The distribution functions of photoexcited electrons (red, thin line) and holes (blue, thin line) after 30 fs (b) and 240 fs (c). Note that for holes the distribution is plotted by the absolute values (reversed in sign) to provide a direct comparison to electrons. Shaded, thicker lines represent the corresponding Fermi–Dirac fits. The fitting parameters, including the goodness of fit (R_e^2, R_h^2), temperature (T_e, T_h), and chemical potential (μ_e, μ_h), are labeled next to the fitted curves.

3.3. Photoexcited carrier thermalization in $PtTe_2$

The evolution of the carrier distribution in monolayer $PtTe_2$, however, exhibits significant differences compared to graphene. Figure 3 illustrates $f_{\mathrm{exci}}(\varepsilon,t)$ at several different time steps for monolayer $PtTe_2$ exposed to a 1.5-eV laser. The dashed vertical lines mark the region from −1.5 eV to 1.5 eV

(setting the valence band maximum as the energy zero), corresponding to the single-photon absorption region. Beyond this region lie the overheated electron region (> 1.5 eV) and overheated hole region (< -1.5 eV), as shown in Fig. 3(a).

At the initial stage of laser incidence (30 fs, Fig. 3(a)), almost all excitations occur within the single-photon absorption region. At this point, the excited electrons have already thermalized to a Fermi–Dirac distribution with a tail extending to higher energies, while the holes do not follow the Fermi–Dirac distribution. After that, the excited carriers quickly diverge from the Fermi–Dirac function in both the low- and high-energy regions. Specifically: (i) For the electron, an internal gap develops between 2 eV and 2.5 eV, with excited electrons accumulating around 2.6 eV, forming a small peak (Figs. 3(b)–3(d)). This results in a non-negligible larger number of overheated electrons than what would be expected from a typical Fermi–Dirac high-energy tail. (ii) For the hole, it exhibits a broad and continuous distribution extending from -1.6 eV to -2.8 eV, indicating a remarkably high population of overheated holes. These anomalies persist throughout the simulation period, with both overheated electrons and holes maintaining their presence. We have also calculated this system with all atoms frozen at their equilibrium positions, i.e., with no phonon involved, and found that the thermalization dynamics remains unchanged (Section S4 in the supplementary materials).

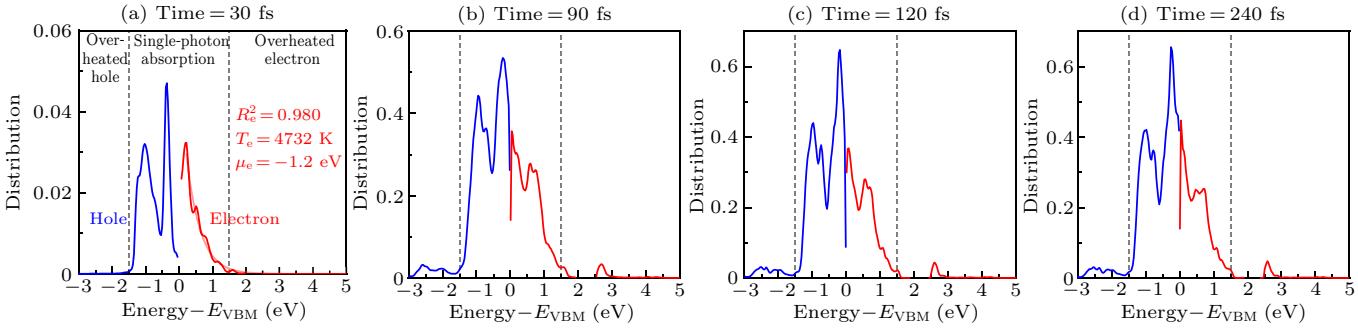


Fig. 3. The distribution functions of photoexcited electrons (red line) and holes (blue line) in monolayer $PtTe_2$. The two vertical dashed lines separate the three regions, i.e., the single-photon absorption, overheated electrons, and overheated holes. Note that only the electron distribution in panel (a) exhibits an obvious Fermi–Dirac behavior, where the Fermi–Dirac fit is shown by a shaded, thicker red line. No other distribution exhibits significant goodness of Fermi–Dirac fit.

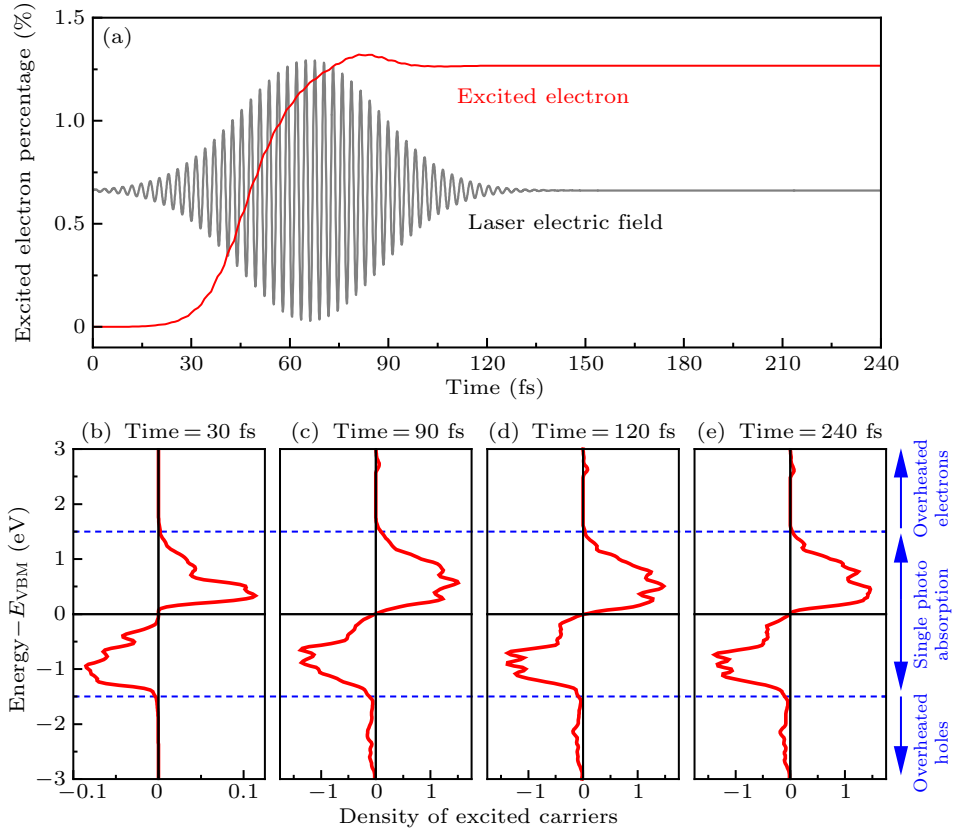


Fig. 4. The time-dependent total number of excited electrons and density of excited electrons in $PtTe_2$, from TDDFT calculations. (a) Total number of excited electrons (red, shown as the percentage relative to all valence electrons) and laser electric field (gray) over time. (b)–(e) Density of excited carriers including electrons (positive values) and holes (negative values) at (b) 30 fs, (c) 90 fs, (d) 120 fs, (e) 240 fs.

Indeed, distribution function $f_{\rm exci}(\varepsilon,t)$ alone is insufficient to fully describe the photoresponse. In fact, the photocurrent is expected to be proportional to the total number of overheated carriers, which directly correlates with the density of excited carriers $D_{\rm exci}(\varepsilon,t)$, the product of the distribution function $f_{\rm exci}(\varepsilon,t)$ and the density of states DOS(ε,t), as derived by Eqs. (4)–(6). To understand the non-trivial thermalization, it is necessary to analyze the detailed dynamics of total number of excited carriers and the $D_{\rm exci}(\varepsilon,t)$. Figure 4(a) shows the percentage of excited electrons relative to the total valence electrons in $PtTe_2$ over time. Under the influence of the oscillating electric field with a Gaussian envelope, electrons are gradually excited from the valence to conduction bands. At the end of the laser (approximately 120 fs), the excitation stabilizes, with approximately 1.3% of the valence electrons transitioning to the conduction band. While, to the best of our knowledge, no direct experimental data has been reported for $PtTe_2$ on the number of ultrafast photoexcited electrons, this value of $\sim 1\%$ is comparable to results for similar compounds reported in previous studies.[64,65] Figures 4(b)–4(e) show the density of excited carriers $D_{\rm exci}(\varepsilon,t)$ at 30 fs, 90 fs, 120 fs, and 240 fs, respectively. Positive values represent excited electrons while negative values correspond to excited holes. At $t = 30$ fs (Fig. 4(b)), the laser field intensity remains low, and the total energy input from laser is relatively small. As a consequence, there are only limited numbers of excited electrons and holes. The photoexcitation occurs predominantly in the single-photon absorption region, indicating energy-conserving, single-particle excitation processes. As the laser intensity increases, a significant number of electron-hole pairs are generated, and $D_{\rm exci}(\varepsilon,t)$ demonstrates non-monotonic behavior at 2.6 eV for electrons and from -1.6 eV to -2.8 eV for holes, the same energy regions as observed in $f_{\rm exci}(\varepsilon,t)$ in Fig. 3. This correlation indicates that the anomalies originate from the excitation processes themselves rather than being an artifact of the density of states. Notably, the number of overheated holes is significantly larger than that of overheated electrons. Such asymmetry between electron and hole is absent in graphene, indicating an asymmetric PTE efficiency for $PtTe_2$ between n-type and p-type heterojunctions.

3.4. The crystal-field splitting and orbital coupling in $PtTe_2$

Now, we discuss the physical mechanism behind such anomalous thermalization.

Firstly, we introduce coupling factor Q to assess the strength of the coupling between two orbitals α and β:

$$Q = 1 - \frac{\left|{\rm proj}_\alpha - {\rm proj}_\beta\right|}{{\rm proj}_\alpha + {\rm proj}_\beta}, \tag{7}$$

where ${\rm proj}_\alpha$ and ${\rm proj}_\beta$ are the projected density of states (PDOS) on orbitals α and β, respectively. By definition, Q ranges from 0 to 1, with larger values indicating stronger orbital coupling.

In $PtTe_2$, the Pt ions are positioned at the center of distorted ($PtTe_6$) octahedra with D_{3d} site symmetry. The schematic diagram of Fig. 5(a) summarizes the hierarchy of crystal-field splitting that lifts the degeneracy of electron states. In a non-distorted octahedron with O_h symmetry, the 5d orbitals of Pt split into t_{2g} and e_g degeneracies. The D_{3d} distortion induces further splitting among the e_g, leading to e_g'', a_{1g}, and e_g' states. The Pt^{4+} ions have a valence electron configuration of $5d^6$, resulting in the energy gap between a_{1g} (VBM) and e_g'' (CBM) states, marked by light blue in Fig. 5(a). Once combined with the ligand configuration of Te^{2-}, the complete orbital configuration near the Fermi level can be described, as shown in Fig. 5(b). The VBM in single-photon absorption region and deeper VB in the overheated hole region consist of d_{xy}, d_{yz}, and d_{xz} orbitals from Pt 5d, bonding with the π orbitals from Te 5p (p_π); the CB in single-photon absorption region has $d_{x^2-y^2}$ and d_{z^2} from Pt, and the σ orbitals from Te 5p (p_σ). Above 2.5 eV (overheated electron region) there exists the s–p coupling which is mainly Pt 6s and Te 5p (p_σ). The orbital configuration in $PtTe_2$ is in distinct differences to that of graphene, the latter of which (Fig. 2(a)) is dominated by a single orbital (p_z) in a large energy region near the Fermi level.

After the laser is turned on, the single-particle optical transitions predominantly occur between the $a_{1g} \rightarrow e_g''$ states, as governed by selection rules and the fact that the VBM is mainly Te 5p orbitals. Consequently, the initially excited electrons and holes are expected to predominantly occupy Te 5p and Pt 5d orbitals, respectively. Now, the differences in thermalization efficiency between electrons and holes can be understood through the distinct orbital coupling mechanisms they follow:

(I) Electrons: Electrons in the low-energy states can thermalize to higher energies via two possible routes. (i) Pt 5d$\rightarrow$Pt 6s. This route is inefficient due to the weak orbital coupling with $Q = 0.33$ between 5d and 6s states. (ii) Pt 5d$\rightarrow$Te 5p$\rightarrow$Pt 6s. For the first step (Pt 5d$\rightarrow$Te 5p), $Q = 0.55$; for the second step (Te 5p$\rightarrow$Pt 6s), $Q = 0.68$. This route involves a two-step process with charge transfer between the ion (Pt) and the ligand (Te), and the efficiency is hence limited. Orbital-projected densities of excited electrons (Figs. 5(c)–5(f)) confirm that the high-energy electrons observed at the 2.6 eV peak reside in the Pt 6s orbital, supporting the explanation above.

(II) Holes: Holes exhibit higher thermalization efficiency because they do not require charge transfer between orbitals for energy redistribution. The low- and high-energy states share the same orbital configuration, primarily derived from Te 5p orbitals. This orbital consistency enables smoother energy transitions and more efficient thermalization.

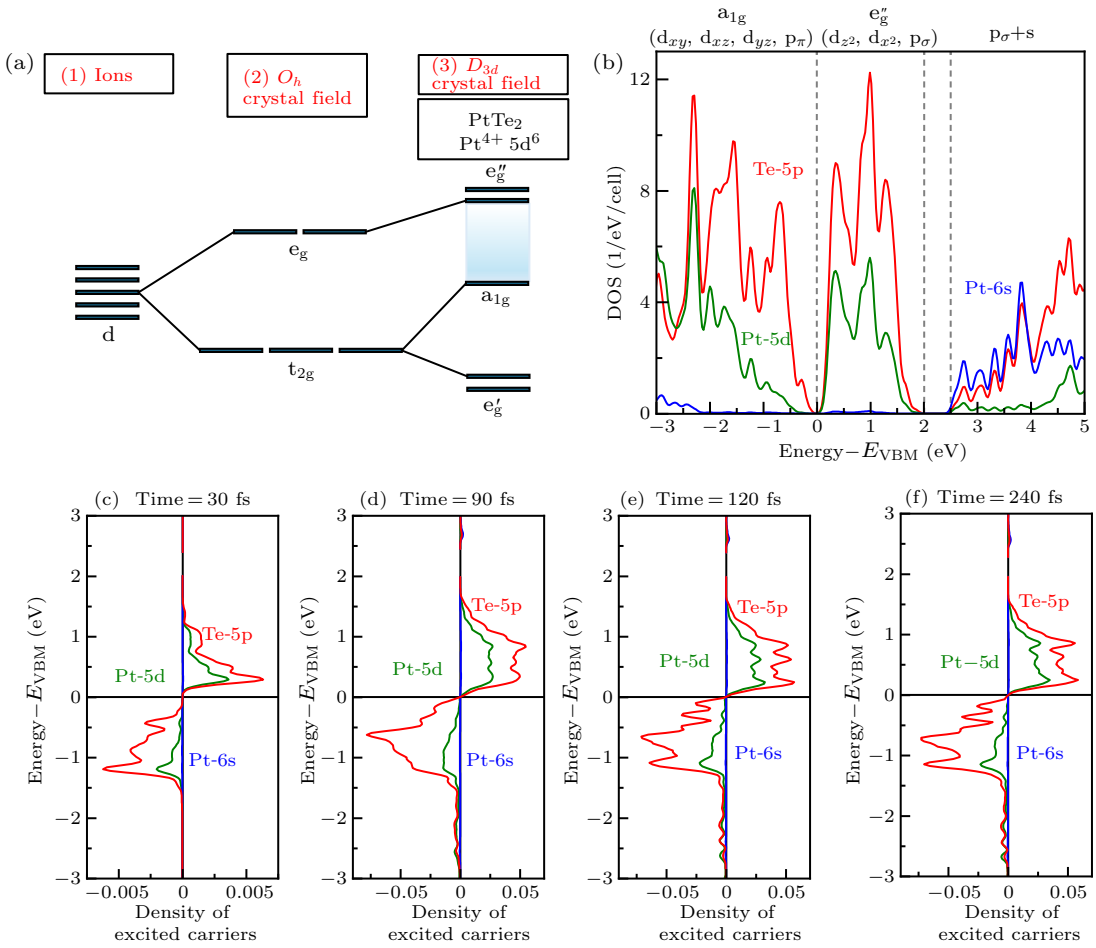


Fig. 5. (a) Schematic diagram of crystal-field splitting in $PtTe_6$ cluster. (b) Ground-state orbital-projected DOS of $PtTe_2$. (c)–(f) Orbital-resolved density of excited carriers in $PtTe_2$ at (c) 30 fs, (d) 90 fs, (e) 120 fs, and (f) 240 fs.

3.5. Design principles for optimal PTE materials

Based on the orbital coupling mechanism discussed above, we propose the following design principles for identifying or engineering compounds with high PTE efficiency. A necessary (but not sufficient) condition for achieving high PTE efficiency is the presence of favorable orbital dynamics that facilitate energy transfer or redistribution. Specifically:

(i) Strong orbital coupling across energy regions

High PTE efficiency can be achieved if there is significant coupling between the primary orbitals in the single-photon absorption region (low-energy states) and those in the target high-energy region. Such coupling ensures efficient energy redistribution and minimizes energy loss during carrier thermalization.

(ii) Orbital consistency across energy regions

Alternatively, if the low- and high-energy regions share the same dominant orbitals, energy redistribution becomes seamless, as no charge transfer or interorbital transitions are required. This condition reduces thermalization bottlenecks, ensuring rapid carrier relaxation and high PTE efficiency.

Such design principles can be used to identify candidate materials, or to apply modifications on the orbital compositions of VBM and CBM in materials lacking inherent orbital coupling or consistency, e.g., doping, strain engineering, or heterostructuring.

Additionally, the physical phenomena observed in materials with stronger orbital coupling, such as $MoSe_2$, can also be explained using the design principles we propose. Compared to $PtTe_2$, theoretical studies[37] have shown that $MoSe_2$ exhibits stronger coupling between Mo 4d and Se 4p orbitals in the CBM to CBM +4 eV range, whereas at higher energies, Mo 5s orbitals exhibit weak coupling to other states. Despite the strong localization of Mo 4d electrons and pronounced many-body effects, excited electrons in $MoSe_2$ exhibit a faster and broader thermalized distribution between CBM and CBM +4 eV, with much weaker thermalization at higher conduction band states. This trend is consistent with the variation in the strength of orbital coupling.

4. Conclusion and perspectives

In this study, we employed rt-TDDFT to investigate the ultrafast thermalization dynamics of photoexcited carriers in monolayer graphene and $PtTe_2$, revealing the fundamental mechanisms driving PTE and outlining design principles for optimizing material performance. In graphene, carriers rapidly thermalize into Fermi–Dirac distributions within ul-

trafast timescales, consistent with experimental results and indicative of efficient energy redistribution. In $PtTe_2$, however, carrier distributions exhibit marked deviations from Fermi–Dirac behavior, characterized by persistent high-energy tails resulting from unique orbital coupling mechanisms. These findings establish the critical role of orbital interactions in shaping ultrafast dynamics, and provide design principles for identifying or engineering high-efficiency PTE materials based on orbital coupling and consistency. This study advances the understanding of ultrafast carrier dynamics, highlights the limitations of conventional thermalization models, and underscores the need for material-specific considerations in designing next-generation photoelectronic devices.

Acknowledgements

Project supported by the Natural Science Foundation of Chongqing of China (Grant No. CSTB2023NSCQ-LZX0087) and the National Natural Science Foundation of China (Grant Nos. 62074021 and 12174380).

References

[1] Scales C and Berini P 2010 *IEEE J. Quantum Electron.* **46** 633
[2] Grajower M, Levy U and Khurgin J B 2018 *ACS Photon.* **5** 4030
[3] Vabbina P, Choudhary N, Chowdhury A A, Sinha R, Karabiyik M, Das S, Choi W and Pala N 2015 *ACS Appl. Mater. Interfaces* **7** 15206
[4] Wang X, Cheng Z, Xu K, Tsang H K and Xu J B 2013 *Nat. Photon.* **7** 888
[5] Li X, Zhu M, Du M, Lv Z, Zhang L, Li Y, Yang Y, Yang T, Li X, Wang K, Zhu H and Fang Y 2015 *Small* **12** 595
[6] Yu W, Li S, Zhang Y, Ma W, Sun T, Yuan J, Fu K and Bao Q 2017 *Small* **13** 1700268
[7] Zeng L, Wu D, Jie J, Ren X, Hu X, Lau S P, Chai Y and Tsang Y H 2020 *Adv. Mater.* **32** 2004412
[8] Zeng L, Han W, Ren X, Li X, Wu D, Liu S, Wang H, Lau S P, Tsang Y H, Shan C X and Jie J 2023 *Nano Lett.* **23** 8241
[9] Allen P B 1987 *Phys. Rev. Lett.* **59** 1460
[10] Massicotte M, Schmidt P, Vialla F, Watanabe K, Taniguchi T, Tielrooij K J and Koppens F H L 2016 *Nat. Commun.* **7** 12174
[11] Fu S, du Fossé I, Jia X, Xu J, Yu X, Zhang H, Zheng W, Krasel S, Chen Z, Wang Z M, Tielrooij K J, Bonn M, Houtepen A J and Wang H I 2021 *Sci. Adv.* **7** eabd9061
[12] Paul K K, Kim J H and Lee Y H 2021 *Nat. Rev. Phys.* **3** 178
[13] Peng L, Liu L, Du S, Bodepudi S C, Li L, Liu W, Lai R, Cao X, Fang W, Liu Y, Liu X, Lv J, Abid M, Liu J, Jin S, Wu K, Lin M L, Cong X, Tan P H, Zhu H, Xiong Q, Wang X, Hu W, Duan X, Yu B, Xu Z, Xu Y and Gao C 2022 *InfoMat* **4** e12309
[14] Johannsen J C, Ulstrup S, Cilento F, Crepaldi A, Zacchigna M, Cacho C, Turcu I C E, Springate E, Fromm F, Raidel C, Seyller T, Parmigiani F, Grioni M and Hofmann P 2013 *Phys. Rev. Lett.* **111** 027403
[15] Gierz I, Petersen J C, Mitrano M, Cacho C, Turcu I C E, Springate E, Stöhr A, Köhler A, Starke U and Cavalleri A 2013 *Nat. Mater.* **12** 1119
[16] Lui C H, Mak K F, Shan J and Heinz T F 2010 *Phys. Rev. Lett.* **105** 127404
[17] Block A, Liebel M, Yu R, Spector M, Sivan Y, García de Abajo F J and van Hulst N F 2019 *Sci. Adv.* **5** eaav8965
[18] Wu S and Sheldon M 2023 *Annu. Rev. Phys. Chem.* **74** 521
[19] An M, Song Q, Yu X, Meng H, Ma D, Li R, Jin Z, Huang B and Yang N 2017 *Nano Lett.* **17** 5805
[20] Uehlein M, Weber S T and Rethfeld B 2022 *Nanomaterials* **12** 1655
[21] Carpene E 2006 *Phys. Rev. B* **74** 024301
[22] Shin T, Teitelbaum S W, Wolfson J, Kandyla M and Nelson K A 2015 *J. Chem. Phys.* **143** 194705
[23] Wang X, Nie S, Li J, Clinite R, Clark J E and Cao J 2010 *Phys. Rev. B* **81** 220301
[24] Kim R, Perebeinos V and Avouris P 2011 *Phys. Rev. B* **84** 075449
[25] Sadasivam S, Chan M K Y and Darancet P 2017 *Phys. Rev. Lett.* **119** 136602
[26] Riffe D M and Wilson R B 2023 *Phys. Rev. B* **107** 214309
[27] Nielsen D O, Van de Walle C G, Pantelides S T, Schrimpf R D, Fleetwood D M and Fischetti M V 2023 *Phys. Rev. B* **108** 155203
[28] Girotto N, Caruso F and Novko D 2023 *J. Phys. Chem. C* **127** 16515
[29] Riffe D M and Wilson R B 2024 *Phys. Rev. B* **109** 184310
[30] Saavedra J R M, Asenjo-Garcia A and García de Abajo F J 2016 *ACS Photon.* **3** 1637
[31] Caruso F, Novko D and Draxl C 2020 *Phys. Rev. B* **101** 035128
[32] Perfetto E and Stefanucci G 2023 *Nano Lett.* **23** 7029
[33] Modine N A and Hatcher R M 2015 *J. Chem. Phys.* **142** 204111
[34] Wang Z, Li S-S and Wang L-W 2015 *Phys. Rev. Lett.* **114** 063004
[35] Silaeva E P, Bevillon E, Stoian R and Colombier J P 2018 *Phys. Rev. B* **98** 094306
[36] Volkov M, Sato S A, Schlaepfer F, Kasmi L, Hartmann N, Lucchini M, Gallmann L, Rubio A and Keller U 2019 *Nat. Phys.* **15** 1145
[37] Schumacher Z, Sato S A, Neb S, Niedermayr A, Gallmann L, Rubio A and Keller U 2023 *Proc. Natl. Acad. Sci.* **120** e2221725120
[38] Kachan E, Tsaturyan A, Stoian R and Colombier J P 2023 *Eur. Phys. J. Spec. Top.* **232** 2241
[39] Shang N Z, Huang C, Chen Q, Liu C, Yao G J, Sun Z P, Meng S, Liu K H and Hong H 2024 *Sci. Bull.* **69** 2522
[40] Hwang E H, Hu B Y K and Das Sarma S 2007 *Phys. Rev. B* **76** 115434
[41] Breusing M, Kuehn S, Winzer T, Malić E, Milde F, Severin N, Rabe J P, Ropers C, Knorr A and Elsaesser T 2011 *Phys. Rev. B* **83** 153410
[42] Tielrooij K J, Song J C W, Jensen S A, Centeno A, Pesquera A, Zurutuza Elorza A, Bonn M, Levitov L S and Koppens F H L 2013 *Nat. Phys.* **9** 248
[43] Brida D, Tomadin A, Manzoni C, Kim Y J, Lombardo A, Milana S, Nair R R, Novoselov K S, Ferrari A C, Cerullo G and Polini M 2013 *Nat. Commun.* **4** 1987
[44] Nie Z, Long R, Sun L, Huang C C, Zhang J, Xiong Q, Hewak D W, Shen Z, Prezhdo O V and Loh Z H 2014 *ACS Nano* **8** 10931
[45] Rohde G, Stange A, Müller A, Behrendt M, Oloff L P, Hanff K, Albert T J, Hein P, Rossnagel K and Bauer M 2018 *Phys. Rev. Lett.* **121** 256401
[46] Weber S T and Rethfeld B 2019 *Phys. Rev. B* **99** 174314
[47] Lloyd-Hughes J, Oppeneer P M, Pereira dos Santos T, *et al.* 2021 *J. Phys.: Condens. Matter* **33** 353001
[48] de Vos E W, Neb S, Niedermayr A, Burri F, Hollm M, Gallmann L and Keller U 2023 *Phys. Rev. Lett.* **131** 226901
[49] Taghinejad M, Xia C, Hrton M, Lee K T, Kim A S, Li Q, Guzelturk B, Kalousek R, Xu F, Cai W, Lindenberg A M and Brongersma M L 2023 *Science* **382** 299
[50] Ma J, Wang Z and Wang L W 2015 *Nat. Commun.* **6** 10107
[51] Liu H W, Liu W H, Suo Z J, Wang Z, Luo J W, Li S S and Wang L W 2022 *Proc. Natl. Acad. Sci.* **119** e2122534119
[52] Liu W H, Gu Y X, Wang Z, Li S S, Wang L W and Luo J W 2023 *Phys. Rev. Lett.* **130** 146901
[53] Perdew J P, Burke K and Ernzerhof M 1996 *Phys. Rev. Lett.* **77** 3865
[54] Baskin Y and Meyer L 1955 *Phys. Rev.* **100** 544
[55] Li J, Kolekar S, Ghorbani-Asl M, Lehnert T, Biskupek J, Kaiser U, Krasheninnikov A V and Batzill M 2021 *ACS Nano* **15** 13249
[56] Charlier J C, Gonze X and Michenaud J P 1991 *Phys. Rev. B* **43** 4579
[57] Zakharchenko K V, Katsnelson M I and Fasolino A 2009 *Phys. Rev. Lett.* **102** 046808
[58] Li C, Debnath B, Tan X, Su S, Xu K, Ge S, Neupane M R and Lake R K 2018 *Carbon* **138** 451
[59] Luo B, Yao Y, Tian E, Song H, Wang X, Li G, Xi K, Li B, Song H and Li L 2019 *Proc. Natl. Acad. Sci.* **116** 17213
[60] Villaos R A B, Crisostomo C P, Huang Z Q, Huang S M, Padama A A B, Albao M A, Lin H and Chuang F C 2019 *npj 2D Mater. Appl.* **3** 2
[61] Lin M K, Villaos R A B, Hlevyack J A, Chen P, Liu R Y, Hsu C H, Avila J, Mo S K, Chuang F C and Chiang T C 2020 *Phys. Rev. Lett.* **124** 036402
[62] Zhang J, Xie Y, Hu Y and Shao H 2020 *Appl. Surf. Sci.* **532** 147387
[63] Shahrokhi M 2017 *Diamond Relat. Mater.* **77** 35
[64] Liu W H, Luo J W, Li S S and Wang L W 2020 *Phys. Rev. B* **102** 184308
[65] Liu W H, Luo J W, Li S S and Wang L W 2022 *Phys. Rev. B* **105** 224306